Simple Holographic Patterning for High-Aspect-Ratio Three-Dimensional Nanostructures with Large Coverage Area

*Ishan Wathuthanthri, Yuyang Liu, Ke Du, Wei Xu, and Chang-Hwan Choi**

Using the vertical standing wave phenomena commonly regarded as a deterrent in holographic lithography, multifaceted three-dimensional (3D) nanostructures are fabricated on polymeric photoresist materials using a simple two-beam interferometer. Large-area 3D nanostructures with high aspect ratios (greater than 10) are readily produced using this methodology, including grating, pillar and pore patterns. Furthermore, manipulation of the lithography process conditions results in unique sidewall profiles of the nanostructures. Such 3D holographic control even produces highly porous polymer membranes composed of 3D interconnected pore networks, which resembles the 3D photonic crystal compound nanostructures that were previously attainable only with limited pattern coverage area using complex multibeam holographic lithography processes. Such well-tailored high-aspect-ratio 3D nanostructures with large pattern coverage area further enable the fabrication of novel nanostructures for functionalized materials via various additive and subtractive pattern transfer techniques such as etching, deposition, and molding. In particular, direct molding followed by thermal decomposition process leads to the synthesis of hierarchical titanium oxide nanostructures of tunable 3D geometry, which would be of great significance in applications of photonic crystals, photovoltaic solar cells, and photocatalyst in water decontamination.

1. Introduction

High-aspect-ratio three-dimensional (3D) nanostructures with subvisible wavelength scale pattern periodicity have gained a lot of interest due to the wide range of applications in photonics,[1–4] phononics,[5] micro/nano fluidics,[6–8] sensing,[9,10] and mechanical structures.[11] Two common approaches used to fabricate such dense-array nanostructures have included phase-shift photolithography[7,12,13] and multibeam holographic lithography (also known as interference lithography),[14] each with its own drawbacks. Phase-shift photolithography relies on the use of a predefined phase-shift mask for the pattern transfer and replication. The pattern periodicity is determined by that of the features defined on the phase-shift mask, typically requiring multiple phase-shift masks for the fabrication of different pattern periodicities. Moreover, it still requires complicated fabrication processes to prepare the initial phase-shift mask with well-defined nanopatterns on it, increasing fabrication steps, complexity, and costs. To alleviate such issues, the fabrication of simple low-cost phase-shift mask layer or material has recently been explored, such as self-assembly of colloidal nanospheres.[15] However, the large-area uniformity of the mask pattern and subsequently the large-area fabrication capabilities (i.e., pattern transfer through such an irregular mask layer) remain a concern. On the other hand, while multibeam holographic lithography techniques are capable of producing highly ordered 3D nanometer-scale features, they require three or more beams to provide the complicated multidimensional interference of light through the material, necessitating intricate optical system design. Such multibeam systems also require careful and time-consuming realignment of the optical path when different pattern periodicities should be fabricated. In addition, optical coherence and power limitations associated with the laser source and the system configuration reduce the maximum pattern coverage area, typically only to the order of mm^2, precluding many practical applications needing large pattern coverage of the nanostructures. Ideally, a simple two-beam interference system capable of forming 3D structures would then be of great interest as it can overcome many of the limitations imposed by a multibeam setup. While previous work using two-beam interference had successfully demonstrated 3D fabrication capabilities, issues of substrate orientation sensitivity and quantity of exposures remain a concern.[16,17]

To alleviate such issues, in this study, we introduce an alternate simple holographic patterning method using only two-beam interference, which allows for the fabrication of large-area 3D holographic nanopatterning with the novel control of the vertical standing wave interference patterns. Contrary to multibeam interferometers that have practical issues such as

I. Wathuthanthri, Dr. Y. Liu, K. Du, W. Xu, Prof. C.-H. Choi
Department of Mechanical Engineering
Stevens Institute of Technology
Castle Point on Hudson
Hoboken, NJ 07030, USA
E-mail: Chang-Hwan.Choi@stevens.edu

DOI: 10.1002/adfm.201201814

complexity and throughput, two-beam interferometers, such as the Lloyd-mirror along with its variations,[18–22] the tunable two-mirror,[23] and the Mach-Zehnder interferometer[18] have successfully shown the capability of fast and convenient periodic tuning while covering a large sample area, resulting in highly reproducible nanostructures over a full wafer scale (100 cm^2). The key idea explored in the fabrication of 3D nanostructures with the two-beam interference lithography processes is the use of a vertical standing wave reflected off from the substrate. Furthermore, in addition to the effects of lithographic process parameters on the geometric three-dimensionality of the fabricated nanostructures, the applications of the high-aspect-ratio 3D polymeric nanostructures for various pattern transfer processes are demonstrated, paving the way for the effective design and fabrication of complex 3D nanostructures for a wide range of materials including polymers, ceramics, and metals.

2. Fabrication Scheme and Process

Figure 1a shows the schematic of the two-beam interferometer used for the experiment. It is based on a Lloyd-mirror configuration where the interference of two beams is provided by the reflection of one beam by the flat mirror which is typically

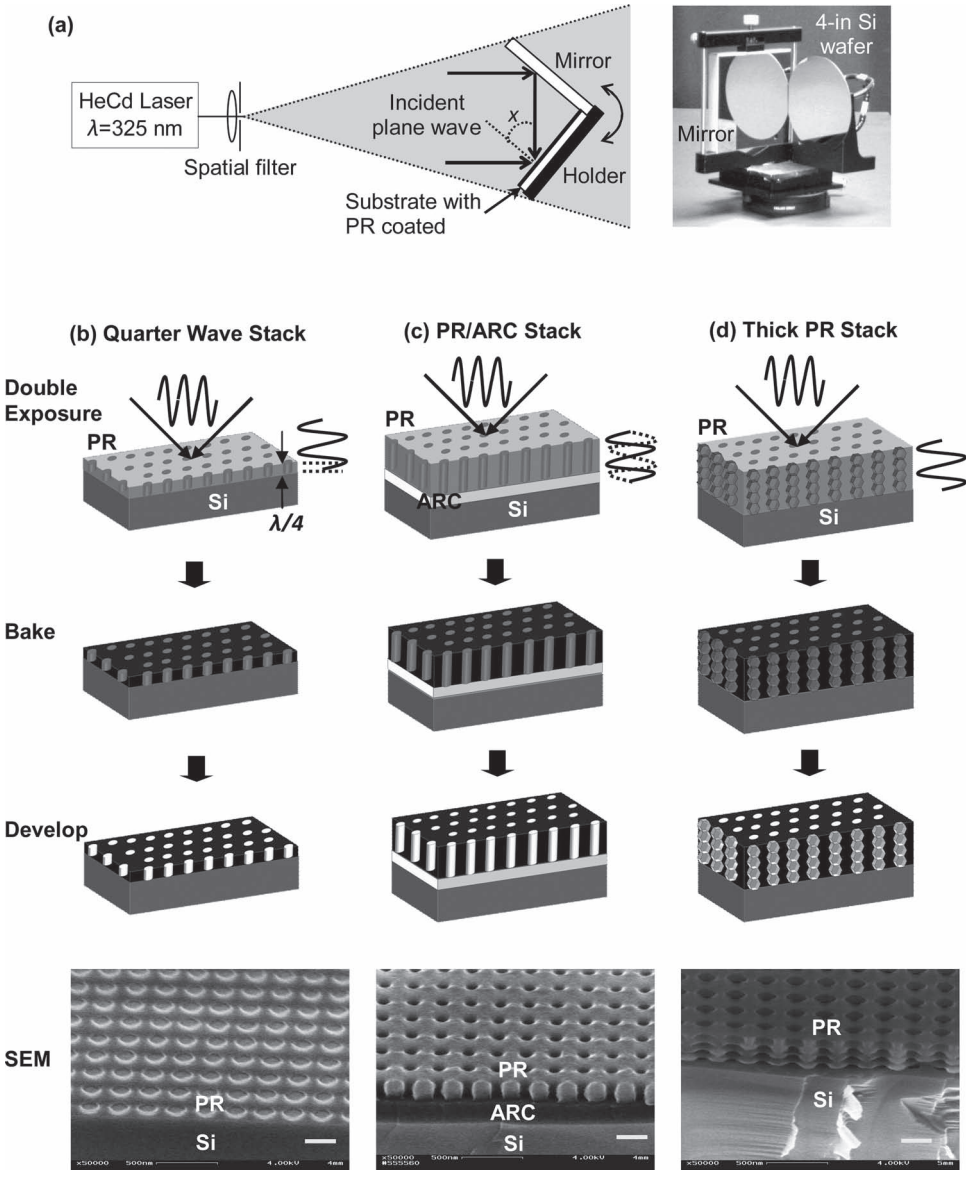

Figure 1. a) Schematic of the two-beam Lloyd-mirror interferometer. b–d) Holographic lithography processes with three different configurations of photoresist (PR) layer. b) Quarter wavelength thick stack; c) ARC/PR stack; d) thick single layer PR and the typical sidewall profiles generated by the processes. Scale bar in the scanning electron microscope (SEM) images is 250 nm.

aligned perpendicular to the substrate.[22] Then, the angle between two interference beams (x) is modulated by rotating the sample stage on which the mirror and substrate holder are placed. The interference of two coherent beams results in the formation of two standing waves in the horizontal and vertical directions, generally registered on a photosensitive polymer film such as photoresist (PR). The working principles of holographic lithography have long been known.[24–26] The horizontal wave is generally regarded as the major wave as it determines the periodicity of the interference fringes along the substrate. The pattern periodicity of the interference fringes (p) depends on the angular variation (x) and the wavelength of the laser (λ) such as $p = \lambda/(2\sin(x))$. A single exposure by two-beam interference produces one dimensional grating patterns, while double exposures with an interim rotation of the substrate is capable of producing grid (pillar or pore) patterns of varying lattices.[27,28] Such a simple methodology for the regulation of pattern periodicity makes the Lloyd-mirror system an ideal interferometer for the systematic study in nanometer-scale fabrication.[29,30] The well-ordered uniform nanostructures with a large pattern coverage area attainable by the maskless interference lithography have recently opened the door to many new scientific and engineering applications.[31–36]

On the other hand, when the incoming beams interfere with the reflection from the polymer/substrate interface, a vertical standing wave is generated and registered within the photoresist polymer film along the thickness direction. The vertical standing wave is recorded as a sinusoidal pattern along the sidewall of the polymer nanostructures and regarded as a hindrance. The amplitude of the sinusoidal scalloping pattern is comparable to the lateral dimension of the polymer nanostructures. Thus, it seriously deforms the geometry of the polymer nanostructures and weakens the mechanical robustness of the structures. Such mechanical defects typically cause failure of the lithographic nanometer-scale patterning. For example, high-aspect-ratio nanostructures with the severe sidewall scalloping are prone to collapse during the wet (development and rinsing) processes due to the high capillary forces of the liquid water used in the processes (see Figure S1 in Supporting Information).[37] To overcome such issues, several methods has been adopted to limit the vertical standing wave in the lithography process. These include the control of refractive index (n) of the substrate surface,[38] the control of exposure dosages,[39] the use of a quarter wavelength thickness resist stack (Figure 1b),[24] or a multilayer composite photopolymer stack with an intermediate anti-reflecting coating (ARC) layer (Figure 1c).[40] However, in many cases, such treatments are undesirable and degrade the fabrication efficiency. A substrate with the control of refractive index requires the use of an index matching interlayer such as SiO_2 so that additional processing steps are necessary to remove the index matching layer after the lithography step. The control of exposure dosage normally requires a use of thick resist stack and the effect is quite sensitive to the lithographic configuration, limiting the pattern coverage area. When a single layer of photoresist polymer with a quarter wavelength thickness is only used, the limited thickness cannot allow the fabrication of high-aspect-ratio nanostructures in the plasma etching or lift-off deposition process where the photoresist layer should function as a mask. Although the use of multi-layer thick PR/ARC stack allows the fabrication of high-aspect-ratio nanostructures, it also makes the fabrication process complicated since additional fabrication steps are necessary to open the ARC layer for the direct etching of the substrate material or deposition onto it. Thus, it will be of great benefit if a thick single layer of resist polymer material can directly be patterned by a one-step process via holographic lithography.

On the contrary to the conventional holographic lithography processes, we study the holographic lithography processes that use a single layer of thick photoresist layer (Figure 1d). Instead of suppressing the vertical standing wave, we engineer this phenomenon to design and construct the nanostructures of high-aspect-ratio 3D features with a further control of the process parameters such as exposure dosage and postexposure heat treatment. For the two-beam interferometer, a He-Cd laser (IK3501R-G, Kimmon Electric, λ = 325 nm, 50 mW, 30 cm coherence length) was used a light source. Polished silicon wafers (10 cm) were used as a substrate, where PR material would be spin-coated on. Due to the relative low power of the laser source, a negative-tone polymer (i-line NR7 series, Futurrex Inc.) was chosen as the photoresist material over a corresponding positive resist. A negative resist has a much higher sensitivity than positive resist and it requires less exposure dosage for registering the interference fringe patterns onto the photopolymer material. A lower dosage results in lower exposure time which enhances the throughput of the process while reducing detrimental environment effects such as vibration and heat fluctuation. While single exposure results in a grating array, double exposure with the interim rotation of the substrate by 90° results in a square array of pore or pillar patterns depending on the exposure dosage (Figure S2, Supporting Information).[27] Negative photoresist material requires a post exposure bake to cross-link the photosensitive polymers in the exposed region. When immersed in developing solution (RD6, Futurrex inc.), the cross-linked region remains firm, while the other area is removed leaving the solidified polymer nanostructures. The samples are then rinsed in water and then transferred into methanol immediately with no exposure to air. After the rinsing with methanol, the samples are dried by blowing nitrogen gas. Methanol has lower surface tension than water (22.5 $mN \cdot m^{-1}$ compared with 72 $mN \cdot m^{-1}$ at room temperature). The use of lower surface tension liquid for the final rinsing and dry process enabled us to avoid the mechanical failure (collapsing problem) of the polymer nanostructures caused by the capillary effects (Figure S1, Supporting Information).

Figure 1b–d compares the holographic lithography processes for three different schemes when a square pore array is fabricated on a silicon substrate by double exposures with negative resist material. The fabrication results (250 nm in periodicity) for each case are also shown under the schematics for comparison. When a single photoresist layer of a quarter wavelength thickness is used (Figure 1b), the sidewall scalloping effect does not emerge out because the film thickness is controlled low enough to circumvent the registration of the vertical standing wave along the layer. When an ARC layer is used together with a thick photoresist layer (Figure 1c), the ARC layer absorbs parts of the reflected beam from the substrate and also induces the phase shifting of the beam by π degrees in order to destructively

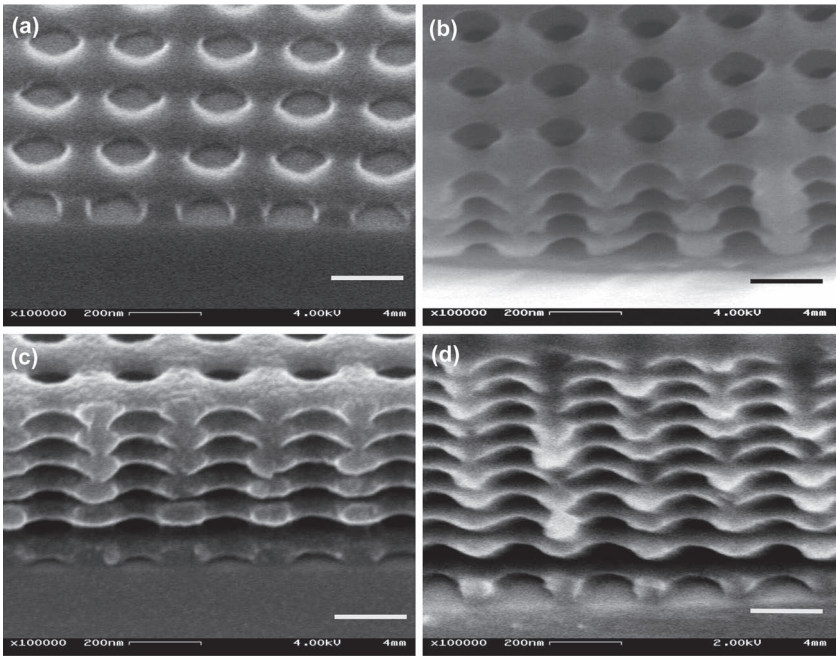

Figure 2. Pore nanostructures with varying aspect ratios. The periodicity of the pore pattern is constant (250 nm) and the thickness of PR layer varies: a) 100 nm; b) 400 nm; c) 600 nm; d) 1000 nm. Scale bar in each SEM image is 200 nm.

interfere with the incoming the beam, resulting in a smooth sidewall. In contrast, when a single thick photoresist layer is used (Figure 1d), the sidewall scalloping is evident along the pore structures, due to the unrestrained vertical standing wave effect. Further detail studies of the 3D sidewall profiles and the applications of this phenomenon to the fabrication of high-aspect-ratio 3D nanostructures are described in the following section.

3. Results and Discussion

3.1. 3D Nanostructures with Varying Aspect Ratios

Figure 2a–d show the pore nanostructures (a square lattice of 250 nm periodicity) fabricated with a single photoresist layer with varying thicknesses (100, 400, 600, and 1000 nm, respectively). The thickness of the photoresist layer was controlled by regulating the concentration of photopolymer solution and the spin speed in coating. The results clearly show the sinusoidal scalloping patterns along the pore walls for the polymer layers that are thicker than a quarter of the wavelength. Even with a thick photoresist layer up to 1000 nm, the 3D sidewall scalloping pattern caused by the vertical standing wave effect is evident. The 3D pore structures with the aspect ratio greater than 10 were readily attainable by using the two-beam holographic patterning. Figure S3 (Supporting Information) also shows the 3D nanostructures of varying aspect ratios, where the pattern periodicity varies while the PR thickness is held constant. The results also clearly show the hierarchical scalloping pattern along the structural sidewalls, for both grating and pore patterns, due to the subvisible wavelength scale vertical standing wave effect.

3.2. Manipulation of Process Conditions

We further investigated the effects of lithographic process parameters on the geometry of the holographic nanostructures and the 3D sidewall profile. The main process conditions that significantly affect the structural formation of negative-tone photopolymer materials are exposure dosage and postexposure heat treatment for chemical amplification. A higher exposure dosage results in the functionalization of more photo-initiators contained in the photopolymer materials, while a higher bake temperature in the postexposure heat treatment process results in the higher rate of cross-linking of the functionalized polymer. This section discusses the effects of exposure dosage and heat treatment on the formation of 3D structures.

3.2.1. Effects of Exposure Dosage

Figure 3 shows two different types of 3D nanopore structures constructed by the control of exposure dosage. Both nanopore structures were made to have the same photoresist thickness (≈1 μm) and pattern periodicity (250 nm). Only the exposure dosage was altered while all the other process parameters were constant. The nanopore structures shown in Figure 3a received a dosage 80% less than that shown in Figure 3b–d are tilted views of the cross-sectioned samples of Figure 3a,b, respectively. Comparing the top views (Figure 3a,b), the pore structures made with a lower exposure dosage (Figure 3a) shows a larger pore size (170 nm) than that (125 nm) with a normal dosage (Figure 3b), while the pattern periodicity remained a constant (250 nm) across both samples. The two-dimensional lateral control of the feature size via exposure dosage is a common process parameter regulated in lithographic process.[40–42] However, the tilted cross-section views (Figure 3c,d) further show the unique structural three-dimensionality and complexity hierarchically added along the pore walls due to the vertical standing wave. Due to the sinusoidal scalloping effects along the pore walls, the pore size does not remain constant along the normal direction but periodically varies. At the location where the intensity of the vertical standing wave is minimum (i.e., every node with half a wavelength), the local exposure dosage is relatively weak so that a larger pose size is formed with the negative-tone photopolymer. Especially, in case of the pore structures with 80% less exposure dosage (Figure 3c), the patternable pore diameter becomes greater than the pattern periodicity at the nodal points so that the pores get merged each other and laterally interconnected at the lateral levels. Meanwhile, each nodal level is still connected through the slender pillar structures left at the lattice (i.e., junction) point where the four pores would meet together. In case of the pore structures with relatively high dosage (Figure 3d), the pore widening effect by the sinusoidal sidewall scalloping pattern

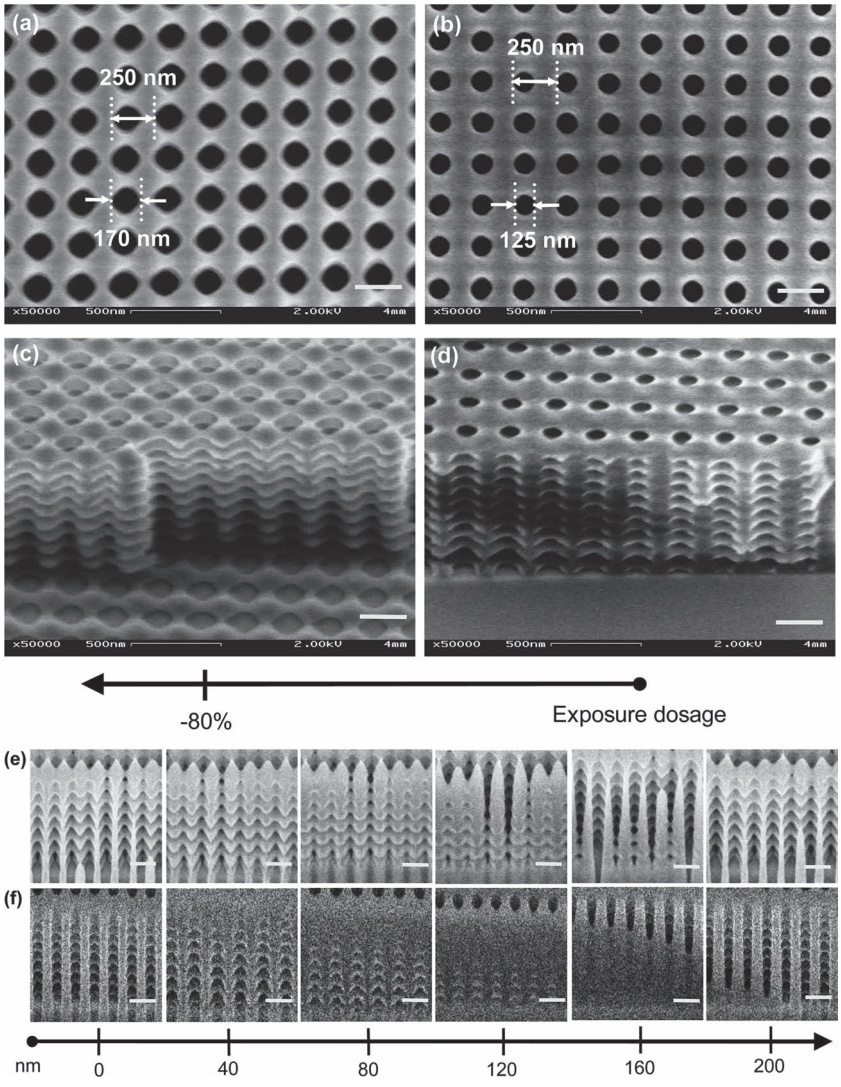

Figure 3. Control of 3D porosity via exposure dosage. a,b) Top-view SEM images of pore nanostructures with underexposed and normal exposure dosages, respectively. (c,d) Cross-sectional titled views of the samples of (a) and (b), respectively. e,f) Cross-sectional titled views with gradual focused ion beam (FIB) milling of the samples of (a) and (b), respectively. Each image in (e,f) is a distance 40 nm apart reveals by the gradual FIB milling. Scale bar in each SEM image is 250 nm.

is less pronounced so that the pores are still isolated by continuous pore walls. Focused ion beam (FIB) milling further validated the distinct porosity and pore networking between the two (Figure 3e,f). Figure 3e,f show the scanning electron microscope (SEM) images of the polymer pore structures shown in Figure 3c,d, respectively, milled by FIB at a distance of every 40 nm apart (see also movies in the Supporting Information). The results demonstrate that the use of vertical standing wave for the formation of 3D scalloping patterns along the structural sidewalls can tune the porosity of the nanopore structures along the pore direction so that both singular and interconnected 3D pores can readily be designed using the simple two-beam holographic lithography process. The interconnected 3D pore structures resemble the photonic crystal compound nanostructures typically fabricated by using complex multibeam holography systems. While such multiple-beam systems are capable of greater control of the 3D lattice structures, the two-beam interferometer can provide the high-aspect-ratio 3D nanoporous layer over a large substrate area (up to a full wafer scale) with greater tunability of the pattern periodicity and simplicity in the system design. Such capabilities would increase the throughput and lower the cost of devices requiring 3D nanostructures such as in photonics crystals, plasmonic sensing, and porous membrane applications.

If the exposure dosage is further decreased, pores are all merged throughout every level so that only pillar structures at the lattice junction area remain. By using such the nonlinearity of the PR pattern along the vertical direction, 3D pillar patterns with scalloped sidewalls can also be conveniently fabricated by using the negative PR as shown in Figure S1d and Figure S2a (Supporting Information).

3.2.2. Effects of Postexposure Heat Treatment

Manipulation of the bake temperature in postexposure heat treatment also resulted in the variation of nanofeature morphology. **Figure 4** shows three different structural morphologies made with varying post exposure bake temperature, while all the other process conditions were kept constant. The lower temperature in the postexposure bake limits the cross-linking of the photo-initiators within the photopolymer. Thus, more photoresist area gets dissolved in the developing process, resulting in the 3D pillar structures (Figure 4a), similar to those obtained

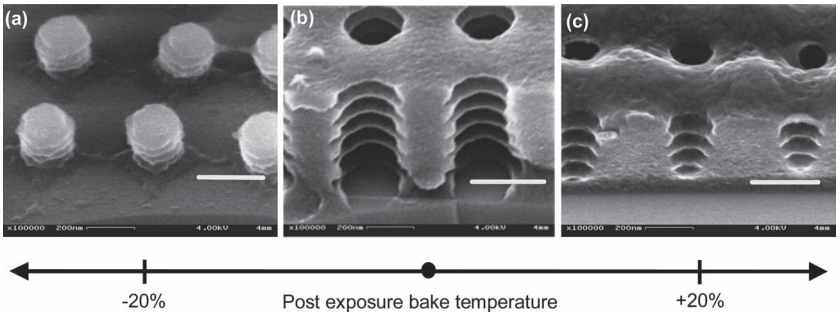

Figure 4. Effects of post exposure bake temperature on the structural three-dimensionality. a) 3D pillar nanostructures. b) 3D porous nanostructures with vertical slope. c) 3D porous nanostructures with positively tapered slope (with a decrease of the pore size along with the pore depth). Scale bar in each SEM image is 200 nm.

with underexposure (Figure S1d, Supporting Information). The result demonstrates that the control of postexposure bake temperature is also capable of generating 3D pillar nanostructures with negative photoresist polymer material, comparable to the results obtained by controlling the exposure dosage. More interestingly, an increase of the postexposure bake temperature (Figure 4c) from the normal condition (Figure 4b) resulted in positively-tapered 3D pore walls. It is attributed to the temperature gradient along the normal direction of the photoresist layer. When the substrate is baked on a hotplate, the photoresist layer closer to the bottom substrate surface becomes hotter than the top layer directly contacting atmosphere in room temperature. Thus, there is a higher rate of cross-linking within the photopolymer near the bottom layer so that less amount of photoresist gets dissolved in the development, resulting in the distinctive positive sidewall slope with the negative photoresist material while still maintaining the 3D hierarchical profile.

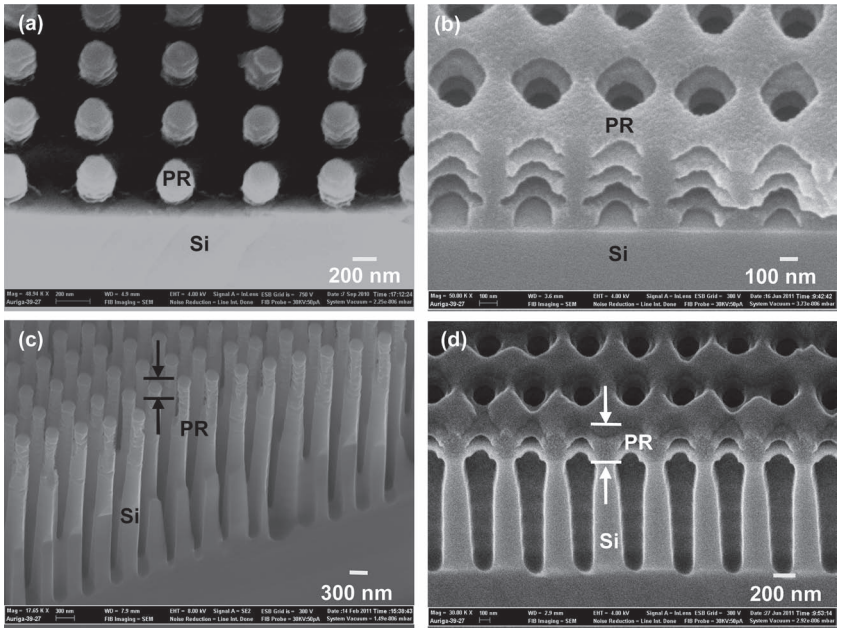

Figure 5. Use of high-aspect-ratio 3D polymer nanopatterns as etch mask in deep reactive ion etching (DRIE). a,b) Pillar and pore photoresist (PR) patterns defined on Si substrates. c,d) Si pillar and pore patterns fabricated by the DRIE using the PR patterns as etch mask. The SEM images show that the PR etch mask layer are still retained on the Si structures even after the high-aspect-ratio DRIE process.

3.3. Applications to Pattern Transfer Processes

While the high-aspect-ratio 3D nanostructures of polymer film as constructed above are of great use for a variety of applications as mentioned previously, the feature of high aspect ratio with 3D nano-dimensional geometry allows the breakthrough in nanofabrication capability and the advancement of developing new functional materials. In this section, three applications to pattern transfer processes are examined, including etching, deposition, and molding via the high-aspect-ratio 3D nanopatterns of polymer material.

3.3.1. High-Aspect-Ratio Etch Mask for Subtractive Deep Reactive Ion Etching

The reductive process of etching silicon substrates with the aid of a photoresist mask is useful for a wide range of non-semiconductor applications. For example, in applications such as nano/micro fluidics,[29,32,36,43] biomaterials,[33,34] template-assisted self-assembly of nanomaterials,[44,45] and high absorption photovoltaic surfaces,[46–49] it is desirable to produce high-aspect-ratio silicon nanostructures as the slender 3D geometry of the nanostructures enhances the performance of these surfaces. Although a quarter wavelength thick single photoresist layer allows the fabrication of high-aspect-ratio silicon nanostructures by deep reactive ion etching (DRIE) process due to its good etch selectivity, it still limits the aspect ratio to less than 10.[29] For other substrate materials such as metals which do not have good etch selectivity to the PR material, a thicker or more etch-resistant etch mask layer is required.[50] The use of a thick multistack PR/ARC layer can alleviate such an issue. However, additional etching steps are generally required to open the ARC layer before the etching of the silicon substrate underneath, which makes the fabrication process complicated.[27,40] In contrast, the thick single layer of high-aspect-ratio polymer nanostructures engineered by the holographic patterning enables a direct and deeper etching of silicon, which makes the fabrication process simpler and more efficient. **Figure 5** shows the fabrication results of the DRIE process using the thick single layer of the high-aspect-ratio 3D polymer nanostructures as a direct etch mask. Figure 5a,b show the pillar and pore patterns of the photoresist, respectively, before the etching. Figure 5c,d then show the fabricated Si nanostructures after the DRIE at cryogenic temperature (–100 °C, see Table S1 in the Supporting Information for detail etch parameters) (Plasmalab 100, Oxford Instruments). The aspect ratio of the silicon nanostructures is ≈20, doubling the previous reported using a single layer of thin photoresist.[29] The SEM images (Figure 5c,d) show the photoresist layer still retained on top of the Si nanostructures, suggesting that further etching is possible in order to obtain the nanostructures with even higher aspect ratios. In this application, the 3D sidewall profile of the polymer nanostructures is inconsequential. It is the high-aspect-ratio geometry that allows the high-aspect-ratio silicon nanostructures in the DRIE. The results suggest that the 3D sidewall profile of the polymer nanostructures has no detrimental effects on the etching process in achieving the high-aspect-ratio deep etching.

3.3.2. High-Aspect-Ratio Deposition Mask for Additive Lift-Off Process

Instead of the reductive etching process for pattern transfer, additive techniques such as physical vapor deposition and

lift-off processes are also capable of forming high-aspect-ratio nanostructures of metals by the use of the polymer nanopatterns as a deposition mask and sacrificial layer. High-aspect-ratio metallic nanostructures of tailored structural dimension and geometry are of great interest to various applications in plasmonics and sensing.[51–53] Although high-aspect-ratio metallic nanostructures can be fabricated by using etching techniques such as inductively couple plasma etching,[50] it requires the use of toxic gases for etchant, which are prohibitive and less cost-effective. Alternatively, direct-writing serial techniques such as e-beam and FIB lithography are capable of fabricating fine metallic features. However, their pattern coverage area is limited due to the slow process characteristics as well as high costs. Therefore, deposition techniques using a simple mask remain an attractive method for the uniform formation of metallic nanostructures.[30,52–54] Similar to etching, it is then desirable to have a high-aspect-ratio single-layer polymer mask that allows the formation of high-aspect-ratio metallic nanostructures while minimizing the lithography steps. **Figure 6** shows the fabrication results of cone-shaped gold (Au) nanostructures by using the single-layer high-aspect-ratio nanoporous polymer membrane for a lift-off process. Figure 6a shows the single layer photoresist stack (600 nm thick) of pore patterns (200 nm in pore diameter) defined on a Si substrate. Figure 6b shows the gold nanostructures deposited through the polymer pore patterns by e-beam evaporation (PVD-75, Kurt J. Lesker Company). As indicated in Figure 6b, the nonuniform step coverage of the deposition over the high-aspect-ratio nanostructures causes the closure of the top holes and results in the formation of the cone-shaped metallic nanostructures with sharp tips. The same phenomenon was observed for different metallic materials made with the polymer nanostructures of various aspect ratios (see Figure S4, Supporting Information). Figure 6c shows the gold nanostructures left on the Si substrate after the removal of the PR layer by using a resist remover solution (RR41, Futurrex Inc.). Figure 6d shows the structural tip of the individual gold nanostructure of the cone shape. The image shows that the gold nanostructure has a radius of curvature <15 nm at the apex of the cone structure, which is less than 10% of the base diameter. The results suggest that the high-aspect-ratio porous polymer nanostructures can conveniently be used to create high-aspect-ratio cone-shaped metal nanostructures with sharpened tips. Such high-aspect-ratio sharp-tip metallic nanostructures are of particular interest in plasmonics and sensing applications as they are capable of concentrating electromagnetic fields into localized hotspots.[55,56] Similar to the etching process, no detrimental effect on the deposition and lift-off processes was observed, caused by the 3D wall profiles of the nanostructures.

3.3.3. High-Aspect-Ratio 3D Template for Direct Molding

In addition to the advantage of the high aspect ratio feature, the 3D nature of the polymer nanostructures can further be utilized to synthesize 3D nanostructured materials integrated with molding techniques. **Figure 7** shows the fabrication of 3D nanostructured layer of titanium oxide (titania, TiO_2) by using the 3D nanoporous polymer film as a replica mold. Titania has high refractive index that is useful for applications in photonic crystals.[14] Titania also has excellent photocatalytic properties making it a useful material for photovoltaic solar cells[57–59] as well as a water oxidation material.[60] Therefore, it is of great importance to be able to create well-tailored 3D nanostructures of titania over a large surface area with high surface to volume ratio for such applications. Figure 7a shows the schematic of a simple molding process developed for the purpose. Initially titania liquid precursor (titanium(IV) ethoxide, $Ti(OC_2H_5)_4$, Sigma-Aldrich) is directly filled into the 3D pore structures of the polymer layer with vacuum desiccation, followed by baking (60 °C), which is used to promote the hydrolysis and condensation of titania precursor. Then, the polymer layer is removed by thermal decomposition in high temperature (575 °C) furnace. The thermal treatment also calcines the titanium(IV) ethoxide into titania, resulting in the formation of titania structures. Figure 7b shows the final fabricated nanostructures of titania when using the 3D porous polymer layer with isolated pores as a mold (similarly to one shown in Figure 3d). The titania pillar structures clearly show the tree-like 3D geometry, which is due to the initial 3D patterns inscribed along the pore walls of the polymer mold layer. Such tree-like 3D features to nanopillar structures are known to result in lowering reflectivity of light in a broad spectral range.[61] The nanostructured surfaces of titania with well-tailored 3D sidewall morphology would be of great interest in applications requiring enhanced light absorption

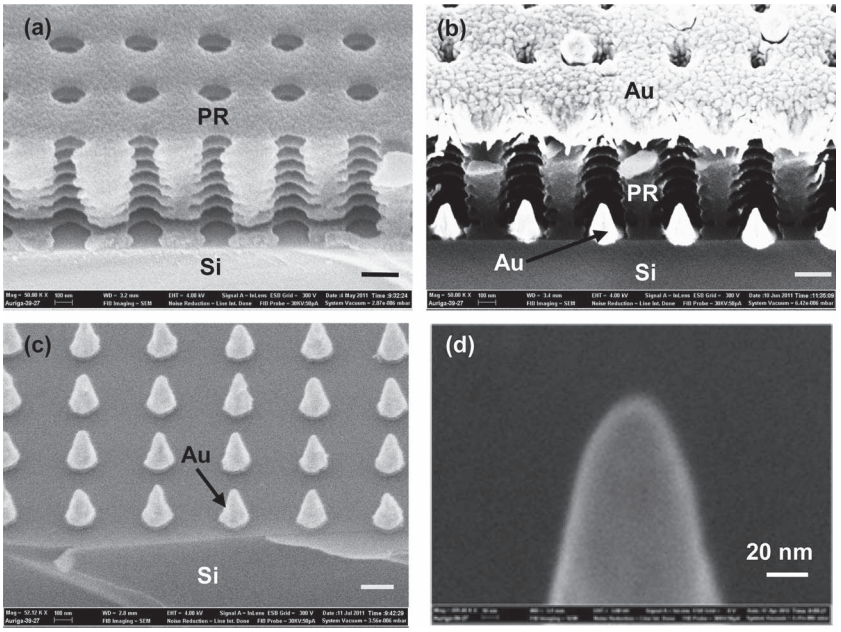

Figure 6. Use of high-aspect-ratio 3D polymer nanopatterns as deposition mask in lift-off process. a) 3D nanoporous photoresist (PR) layer defined on a Si substrate. b) E-beam deposition of gold (Au) layer. c) Removal of the PR layer by lift-off process. d) High magnification SEM image of the sharp tip of the nanocone gold structure. Scale bars in (a–c) are 200 nm.

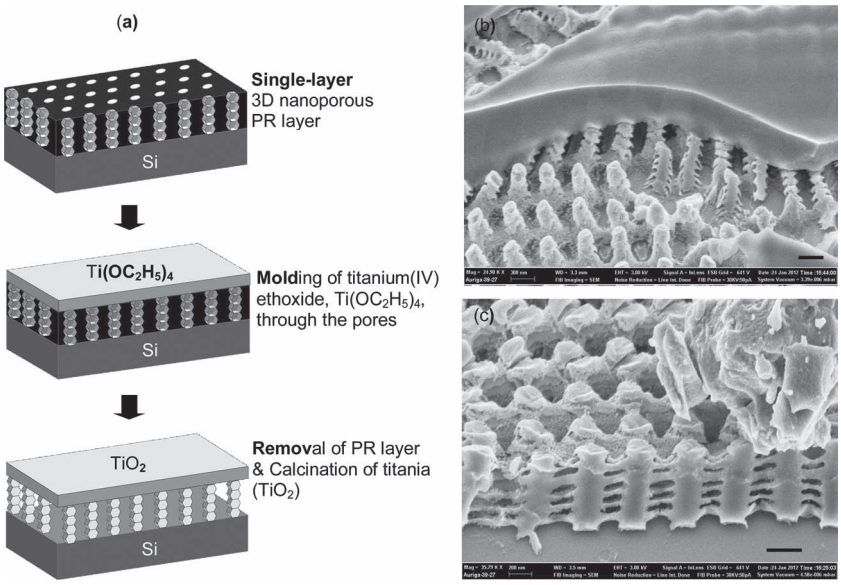

Figure 7. Fabrication of 3D nanostructures of titania (TiO_2) by molding via the 3D nanoporous polymer layer. a) Schematic of the molding process. b) Titania nanostructures fabricated using the nanoporous photoresist (PR) layer with isolated pores similar to the one shown in Figure 3d. c) Titania nanostructures fabricated using the nanoporous PR layer with an interconnected pore network similar to the one shown in Figure 3c. Scale bar in each SEM image (b–c) is 300 nm.

coupled with photocatalyst properties, paving the new way for a highly functionalized material and surface for photovoltaics. In contrast, Figure 7c shows the titania nanostructures made with the 3D porous polymer layer with interconnected pore network (similarly to one shown in Figure 3c). It clearly shows that the titania nanostructures are interconnected to each other and form a mesh. It confirms the 3D interconnectivity of the porous nanostructures of the polymer mold layer, previously verified by FIB milling (Figure 3e).

The molded nanostructures can also be collected as free-standing membrane and further transferred onto another substrate. **Figure 8**a shows the schematic of the new fabrication process. In this process, an ARC layer is used together with the photoresist layer to facilitate the release and pattern transfer of the polymer layer composited with the molded material. In this case, the thickness of ARC layer is regulated so that the effect of suppressing the vertical standing wave is defunct in the holographic patterning of the photoresist layer. As mentioned previously, an ARC layer suppresses the vertical standing wave only when the thickness is designed to phase-shift the reflected beam and to result in deconstructive interference in the vertical direction. When the thickness is mismatched, the ARC layer does not influence the capability of creating 3D wall profiles along the polymer nanostructures in the lithography process. To this end, an ARC layer (XHRiC-16, Brewer Science) of 150 nm thick was used merely as a sacrificial layer to facilitate the release and pattern transfer process. Figure S5 (Suppporting Information) shows no detrimental effect in forming the 3D wall profile along the high-aspect-ratio pore structures as a result of this sacrificial ARC layer. After the titanium(IV) ethoxide film is molded into the 3D nanoporous polymer layer, the entire composite film (including ARC layer, photoresist membrane, and titania) was released from the supporting silicon substrate in H_2O_2 solution,[62] resulting in a free-standing film. The use of only a single layer of photoresist with no aid of the ARC layer could not release the polymer film effectively. It was critical to use the ARC layer in order to provide a robust mechanical platform as well as a functional layer for the separation. Then, the solution was gradually replaced with de-ionized water and the free-standing composite film was transferred onto another silicon substrate in water. When it is transferred, the film can be flipped so that the direction of the molded nanostructures can be reversed in order for the pillar structures to protrude out. Then, the sample was dried in ambient

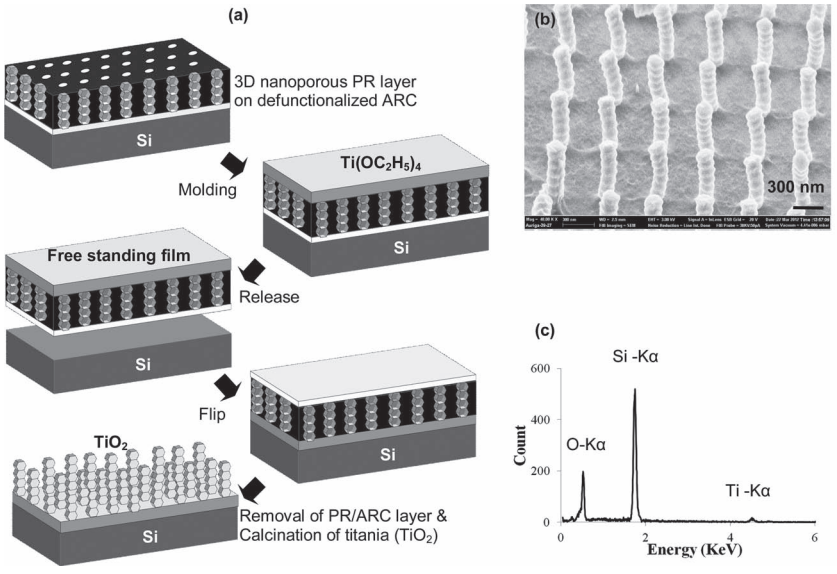

Figure 8. Fabrication of 3D nanostructures of titania (TiO_2) by molding followed by reverse pattern transfer. a) Schematic of the fabrication process, where the molded layer is released as a free-standing film and transferred to any substrate for pattern transfer. During the pattern transfer it can be flipped to reverse the direction of nanostructures. In this process, the ARC layer is mainly used as rigid support for the release and sacrificial etching steps. The effect of suppressing the vertical standing wave of the ARC layer is modulated with the control of the film thickness so that the 3D scalloping wall profiles can still be reserved. b) Fabricated free-standing titania nanostructures transferred on a new Si substrate. c) Energy dispersive spectroscopy (EDS) measurement of the titania nanostructures, showing Kα spikes corresponding to Ti, O, and Si.

conditions and followed the thermal treatment to remove the PR/ARC layers and calcinate the titania. Figure 8b shows the final fabricated nanostructures of 3D titania transferred onto a new Si substrate by using the film transfer process. Using the 3D polymer layer containing the isolated pores (such as the one shown in Figure 3d), disconnected pillar structures of titania with 3D sidewall profile was successfully fabricated. To verify the material composition of the titania molded through the process, X-ray spectra of energy dispersive spectroscopy (EDS) was measured. Figure 8c shows the spectra measured for the nanopillared titania samples (Figure 8b). The result shows Kα spikes at ≈4.5 KeV (Ti) and ≈0.5 KeV (O), proving the formation of titania. The Kα peak at ≈1.7 KeV represents the Si substrate on which the transferred film was placed.

These results demonstrate that the high-aspect-ratio 3D polymer nanostructures with tailored 3D porosity can serve as an efficient template to construct various types of 3D nanostructures of novel materials by the direct molding process further integrated with various pattern transfer techniques with the added benefit of large-scale manufacturability.

4. Conclusions

In this study, an efficient holographic nanopatterning procedure to create high-aspect-ratio 3D nanostructures of polymeric photoresist material has successfully been demonstrated, using a simple two-beam interferometer system that can expose large substrate area up to a full wafer-scale. Using the vertical standing wave phenomenon associated with the interference lithography process, the high-aspect-ratio 3D nanostructures are readily producible with additional controllability of their nanometer-scale geometry by the regulation of lithographic processing parameters such as exposure dosage and postexposure heat treatment for the photopolymer. While such polymeric nanostructures of well-tailored 3D geometry with large coverage area are useful in many scientific and engineering applications for themselves, they also enable to simplify many nanofabrication and material processes including both subtractive, additive, and rapid prototyping processes such as etching, deposition, molding, and pattern transfer. The combined features of the structural high aspect ratio and geometric three-dimensionality are still attainable in such pattern transfer processes, resulting in the design of novel 3D nanostructures with tailored material properties for potential customized applications in micro/nano fluidics, membranes, biomaterials, tissue engineering, photovoltaics, plasmonics and sensing.

5. Methods and Materials

Lloyd-Mirror Two-Beam Interferometry: The Lloyd-mirror interferometer was constructed on a 1.2 m × 2.4 m optical table. A HeCd laser of continuous wave (CW) mode with the wavelength of 325 nm and, power of 50 mW, and coherence length of 30 cm (IK3501R-G, Kimmon Electric) was used for a laser source. The beam was spatially filtered and expanded to a distance of 1.8 m guaranteeing an electric field and intensity distribution greater than 0.9 and 0.8, respectively, at the sample stage. The beam diameter at the stage was ≈30 cm, and the power was ≈50 μW. The reflecting mirror was 10 cm × 10 cm with a UV enhanced aluminum coating (Edmund Optics) for high reflectance at a wide range of angles.

Holographic Lithography: All photopolymer material used in this paper was a negative tone photoresist (NR7 series, Futurrex Inc.). For holographic patterning, polished silicon wafers (10 cm in diameter) were first prepared by cleaning with acetone, methanol, and de-ionized water, followed by blow-dry with nitrogen gas. Then, the photoresist polymer solution was spin-coated on the silicon substrate for desired film thickness. By regulating the photopolymer concentration and the spin speed of the solution, the film thickness ranges from 100 to 1000 nm. Following the spin coating, the substrates were soft-baked on a hot plate at 150 °C for 1 min to dehydrate. Samples were then exposed using the laser interference system for the desired structure formation, with the dose ranging from 5 to 15 mJ/cm^2. Following exposure, the substrates were baked for postexposure heat treatment (chemical amplification) on a hotplate at 100 °C for 1 min. The substrates were then immersed in developing solution for 10 s (RD6, Futurrex Inc.) to obtain the lithography patterns. Then, the substrates were rinsed with de-ionized water for 30 s followed by methanol for 5 s with no exposure to air during the transition. Finally, the substrates were dried by blowing nitrogen gas.

Deep Reactive Ion Etching: For the deep reactive ion etching (DRIE) of silicon substrates, a cryogenic etch mode was used at –100 °C (Plasmalab 100, Oxford Instruments). O_2 and SF_6 were used for etching gases for cryogenic process (see Table S1 in Supporting Information for detailed flow rates and plasma power levels). The number of etching cycle in the cryogenic process was varied according to the etch depth desired.

Lift-Off Process: E-beam evaporation (PVD-75, Kurt J. Lesker Company) was used for the deposition of metal films through the photoresist nanopatterns. The base pressure of the evaporator chamber was set at ≈1.33×10^{-5} Pa. The deposition rate for the metals (Au and Ag) was regulated to be 0.2 nm/s. During the deposition, the chamber pressure was maintained below 1.33×10^{-3} Pa range. Following the deposition, the photoresist layer was removed by immersing the sample in resist remover (RR41, Futurrex Inc.) for 20 min at 100 °C heated on a hotplate.

Titania Molding and Film Transfer: Titanium(IV) ethoxide ($Ti(OC_2H_5)_4$, Sigma-Aldrich) was used as titania (TiO_2) precursor. Titanium(IV) ethoxide was used as received without further purification. For molding into the photoreisist polymer structures, the silicon substrate with the patterned photoresist layer was placed horizontally in a desiccator and then the titanium(IV) ethoxide solution was pored over the photoresist layer to spread out. The desiccator was vacuumed for 30 min to facilitate the filling of titania precursor solution into the nanopatterned photoresist layer. Then, the substrate was baked at 60 °C for 1 h to promote the hydrolysis and condensation of titania precursor in the photoresist layer. For the film transfer process, the substrate was immersed into the aqueous solution of hydrogen peroxide (H_2O_2) (3% in volume), which delaminates the photoresist film supported by a thin ARC layer. As a result, a free-standing composite film (including the ARC and the photoresist layer molded with titania) was obtained. Then, the H_2O_2 solution was gradually replaced with de-ionized water

where the free-standing composite film was manipulated and placed on another silicon substrate for film transfer. Tweezers were used to control the direction and placement of the free-standing film on the target substrate in the film transfer process. Then, the substrate with the transferred composite film was taken out from water and allowed to dry in ambient conditions. For the removal of the polymer layer from the molded titania layer, the substrate was put into a preheated Muffle furnace (575 °C) for 1 h to thermally decompose the polymers. Titania is also calinated in the heat treatment.

Supporting Information

Supporting Information is available from the Wiley Online Library or from the author.

Acknowledgements

This research was carried out in part at the Center for Functional Nanomaterials (CFN), Brookhaven National Laboratory (BNL), which was supported by the U.S. Department of Energy, Office of Basic Energy Sciences, under contract no. DE-AC02-98CH10886. The research effort used microscope resources partially funded by the National Science Foundation through NSF Grant DMR-0922522. The authors thank Dr. Tsengming Chou at Stevens Institute of Technology for the assistance with SEM microscopy and characterization.

Received: July 3, 2012
Published online: September 7, 2012

[1] S. Noda, K. Tomoda, N. Yamamoto, A. Chuinan, *Science* **2000**, *289*, 604–606.
[2] M. Campbell, D. N. Sharp, M. T. Harrison, R. G. Denning, A. J. Turberfield, *Nature* **2000**, *404*, 53–56.
[3] J. Li, G. Liang, X. Zhu, S. Yang, *Adv. Funct. Mater.* **2012**, 10.1002/adfm.201290086.
[4] G. von Freymann, A. Ledermann, M. Thiel, I. Staude, S. Essig, K. Busch, M. Wegener, *Adv. Funct. Mater.* **2010**, *20*, 1038–1052.
[5] T. Gorishnyy, C. K. Ullal, M. Maldovan, G. Fytas, E. L. Thomas, *Phys. Rev. Lett.* **2005**, *94*, 1155011–1155015.
[6] S.-G. Park, J. H. Moon, S.-K. Lee, J. Shim, S.-M. Yang, *Langmuir* **2010**, *26*, 1468–1472.
[7] S. Jeon, J.-U. Park, R. Cirelli, S. Yang, C. E. Heitzman, P. V. Braun, P. J. A. Kenis, J. A. Rogers, *Proc. Natl. Acad. Sci. USA* **2004**, *101*, 12428–12433.
[8] Y.-L. Yang, C.-C. Hsu, T.-L. Chang, L.-S. Kuo, P.-H. Chen, *Appl. Surf. Sci.* **2010**, *256*, 3683–3687.
[9] J. H. Kim, J. H. Moon, S.-Y. Lee, J. Park, *Appl. Phys. Lett.* **2010**, *97*, 1037011–103703.
[10] X. Xiao, G. A. Montano, T. L. Edwards, C. M. Washburn, S. M. Brozik, D. R. Wheeler, D. B. Burckel, R. Polsky, *Biosens. Bioelectron.* **2011**, *26*, 3641–3646.
[11] J.-H. Jang, C. K. Ullal, T. Choi, M. C. Lemieux, V. V. Tsukruk, E. L. Thomas, *Adv. Mater.* **2006**, *18*, 2123–2127.
[12] I. Bita, T. Choi, M. E. Walsh, H. I. Smith, E. L. Thomas, *Adv. Mater.* **2007**, *19*, 1403–1407.
[13] A. M. Bowen, M. J. Motala, J. M. Lucas, S. Gupta, A. J. Baca, A. Mihi, A. P. Alivisatos, P. V. Braun, R. G. Nuzzo, *Adv. Funct. Mater.* **2012**, *22*, 2927–2938.
[14] J.-H. Jang, C. K Ullal, M. Maldovan, T. Gorishnyy, S. Kooi, C. Koh, E. L. Thomas, *Adv. Funct. Mater.* **2007**, *17*, 3027–3041.
[15] C.-H. Chang, L. Tian, W. R. Hesse, H. Gao, H. J. Choi, J.-G. Kim, M. Siddiqui, G. Barbastathis, *Nano. Lett.* **2011**, *11*, 2533–2537.
[16] N. D. Lai, W. P. Liang, H. H. Lin, C. C. Hsu, C. H. Lin, *Opt. Express* **2005**, *13*, 9605–9611.
[17] J. W. Menezes, E. J. de Carvalo, E. S Braga, L. Cescato, *J. Opt. A: Pure Appl. Opt.* **2009**, *11*, 075103–075108.
[18] H. I. Smith, *Physica E* **2001**, *11*, 104–109.
[19] P. Mehrotra, C. W. Holzwarth, R. J. Blaikie, *J. Micro/Nanolithog., MEMS, MOEMS* **2011**, *10*, 033012–033014.
[20] J. de Boor, D. S. Kim, V. Schmidt, *Opt. Lett.* **2010**, *35*, 3450–3452.
[21] J. de Boor, N. Geyer, U. Gösele, V. Schmidt, *Opt. Lett.* **2009**, *34*, 1783–1785.
[22] I. Wathuthanthri, W. Mao, C.-H. Choi, *Opt. Lett.* **2011**, *36*, 1593–1595.
[23] W. Mao, I. Wathuthanthri, C.-H. Choi, *Opt. Lett.* **2011**, *36*, 3176–3178.
[24] N. N Efremow, N. P. Economou, K. Bezjian, S. S. Dana, H. I. Smith, *J. Vac. Sci. Technol., B* **1978**, *19*, 1234–1237.
[25] S. H. Zaidi, S. R. J. Brueck, *Appl. Optics* **1988**, *37*, 2999–3002.
[26] E. Kapon, A. Katzir, *J. Appl. Phys.* **1982**, *53*, 1387–1390.
[27] Y.-J. Hung, S.-L. Lee, Y.-T. Pan, *J. Vac. Sci. Technol., B* **2010**, *28*, 1030–1038.
[28] S. H. Zaidi, S. R. J. Brueck, *J. Vac. Sci. Technol., B* **1993**, *11*, 658–666.
[29] C.-H. Choi, C.-J. Kim, *Nanotechnology* **2006**, *17*, 5326–5333.
[30] K. Du, I. Wathuthanthri, W. Mao, W. Xu, C.-H. Choi, *Nanotechnology* **2011**, *22*, 285306–285313.
[31] D. Xia, Z. Ku, S. C. Lee, S. R. J. Brueck, *Adv. Mater.* **2011**, *23*, 147–179.
[32] C.-H. Choi, U. Ulmanella, J. Kim, C.-M. Ho, C.-J. Kim, *Phys. Fluids* **2006**, *18*, 087105.
[33] C.-H. Choi, S. H. Hagvall, B. M. Wu, J. C. Y. Dunn, R. E. Beygui, C.-J. Kim, *Biomaterials* **2007**, *28*, 1672–1679.
[34] C.-H. Choi, S. H. Hagvall, B. M. Wu, J. C. Y. Dunn, R. E. Beygui, C.-J. Kim, *J. Biomed. Mater. Res.* **2009**, *89A*, 804–817.
[35] K. S. Layland, F. Rofail, S. Heydarkhan, J. M. Gluck, N. P. Ingle, E. Angelis, C.-H. Choi, W. R. MacLellan, R. E Beygui, R. J. Shemin, S. Heydarkhan-Hagvall, *Biomaterials* **2009**, *30*, 4665–4675.
[36] C.-H. Choi, C.-J. Kim, *Langmuir* **2009**, *25*, 7561–7567.
[37] S. F. Chini, A. Amirfazli, *Langmuir* **2010**, *26*, 13707–13714.
[38] E. J. Carvalho, M. A.R. Alves, E. S. Braga, L. Cescato, *Microelectron. J.* **2006**, *37*, 1265–1270.
[39] R. Murillo, H. A. van Wolferen, L. Abelmann, J. C. Lodder, *Microelectron. Eng.* **2005**, *78*, 260–265.
[40] M. Farhoud, J. Ferrera, A. J. Lochtefeld, T. E. Murphy, M. L. Schattenburg, J. Carter, C. A. Ross, H. I. Smith, *J. Vac. Sci. Technol., B* **1999**, *17*, 3182–3185.
[41] A. Fernandez, J. Y. Decker, S. M. Herman, D. W. Phillion, D. W. Sweeney, M. D. Perry, *J. Vac. Sci. Technol., B* **1997**, *15*, 2439–2443.
[42] X. Zhang, M. Theuring, Q. Song, W. Mao, M. Begliarbekov, S. Strauf, *Nano. Lett.* **2011**, *11*, 2715–2719.
[43] C.-H. Choi, C.-J. Kim, *Phys. Rev. Lett.* **2006**, *96*, 066001.
[44] W. Xu, R. Leeladhar, Y.-T. Tsai, E.-H. Yang, C.-H. Choi, *Appl. Phys. Lett.* **2011**, *98*, 073101.
[45] Y.-T. Tsai, W. Xu, E. H. Yang, C.-H. Choi, *Nanosci. Nanotechnol. Lett.* **2010**, *2*, 150–156.
[46] J. Zhu, Z. Yu, G. F. Burkhard, C.-M. Hsu, S. T. Connor, Y. Xu, Q. Wang, M. McGehee, S. Fan, Y. Cui, *Nano. Lett.* **2009**, *9*, 279–282.
[47] J. Zhu, C.-M. Hsu, Z. Yu, S. Fan, Y. Cui, *Nano. Lett.* **2010**, *10*, 1979–1984.

[48] J. Q. Xi, M. F. Schubert, J. K. Kim, E. F. Schubert, M. Chen, S.-Y. Lin, W. Liu, J. A. Smart, *Nat. Photonics* **2007**, *1*, 176–179.
[49] L. Hu, G. Chen, *Nano. Lett.* **2007**, *7*, 3249–3252.
[50] M. F. Aimi, M. P. Rao, N. C. MacDonald, A. S. Zuruzi, D. P. Bothman, *Nat. Mater.* **2004**, *3*, 103–105.
[51] N. C. Lindquist, T. W. Johnson, D. J. Norris, S.-H. Oh, *Nano. Lett.* **2011**, *11*, 3526–3530.
[52] J.-C. Yang, H. Gao, J. Y. Suh, W. Zhou, M. H. Lee, T. W. Odom, *Nano. Lett.* **2010**, *10*, 3173–3178.
[53] H. Gao, J. K. Hyun, M. H. Lee, J.-C. Yang, L. J. Lauhon, T. W. Odom, *Nano. Lett.* **2010**, *10*, 4111–4116.
[54] J. W. Menezes, J. Ferreira, M. J. L. Santos, L. Cescato, A. G. Brolo, *Adv. Funct. Mater.* **2010**, *20*, 3918–3924.
[55] S. Lee, J. Shin, Y.-H. Lee, J.-K. Park, *ACS. Nano* **2010**, *4*, 7175–7184.
[56] F. De Angelis, F. Gentile, F. Mecarini, G. Das, M. Moretti, P. Candeloro, M. L. Coluccio, G. Cojoc, A. Accardo, C. Liberale, R. P. Zaccaria, G. Perozziello, L. Tirinato, A. Toma, G. Cuda, R. Cingolani, E. Di Fabrizio, *Nat. Photonics* **2011**, *5*, 682–687.
[57] D. Wang, L. Liu, F. Zhang, K. Tao, E. Pippel, K. Domen, *Nano. Lett.* **2011**, *11*, 3649–3655.
[58] C. L. Muhich, Y. Zhou, A. M. Holder, A. W. Weimer, C. B. Musgrave, *J. Phys. Chem. C* **2012**, *116*, 10138–10149.
[59] P. Docampo, S. Guldin, M. Stefik, P. Tiwana, M. C. Orilall, S. Huttner, H. Sai, U. Wiesner, U. Steiner, H. J. Snaith, *Adv. Funct. Mater.* **2010**, *20*, 1787–1796.
[60] S. Hoang, S. Guo, N. T. Hahn, A. J. Bard, C. B. Mullins, *Nano. Lett.* **2012**, *12*, 26–32.
[61] C. Yan, X. Li, K. Zhou, A. Pan, P. Werner, S. L. Mensah, A.r T. Vogel, Volker Schmidt, *Nano. Lett.* **2012**, *12*, 1799–1805.
[62] Y. Liu, K. Du, I. Wathuthanthri, W. Xu, C.-H. Choi, in *Proceedings of MEMS 2012: The 25th International Conference on Micro Electro Mechanical Systems*, January 29–February 2, 2012, Paris, France.